nature materials

ARTICLES

PUBLISHED ONLINE: 19 AUGUST 2012 | DOI: 10.1038/NMAT3393

Probing oxygen vacancy concentration and homogeneity in solid-oxide fuel-cell cathode materials on the subunit-cell level

Young-Min Kim[1,2], Jun He[1,3], Michael D. Biegalski[4], Hailemariam Ambaye[5], Valeria Lauter[5], Hans M. Christen[4], Sokrates T. Pantelides[1,3,6], Stephen J. Pennycook[1,3], Sergei V. Kalinin[4] and Albina Y. Borisevich[1]*

Oxygen vacancy distributions and dynamics directly control the operation of solid-oxide fuel cells and are intrinsically coupled with magnetic, electronic and transport properties of oxides. For understanding the atomistic mechanisms involved during operation of the cell it is highly desirable to know the distribution of vacancies on the unit-cell scale. Here, we develop an approach for direct mapping of oxygen vacancy concentrations based on local lattice parameter measurements by scanning transmission electron microscopy. The concept of chemical expansivity is demonstrated to be applicable on the subunit-cell level: local stoichiometry variations produce local lattice expansion that can be quantified. This approach was successfully applied to lanthanum strontium cobaltite thin films epitaxially grown on substrates of different symmetry, where polarized neutron reflectometry revealed a strong difference in magnetic properties. The different vacancy content found in the two films suggests the change in oxygen chemical potential as a source of distinct magnetic properties, opening pathways for structural tuning of the vacancy concentrations and their gradients.

For many applications, the functionality of transition-metal-oxide materials and devices is ultimately determined by the concentration and dynamics of oxygen vacancies. Paradigmatic examples include solid-oxide fuel cells, gas sensors and electrochemical pumps that operate by directing and controlling vacancy flows[1,2]. Ionic phenomena underpin the operation of emergent information-technology devices such as memristive and electroresistive memories and logic[3,4]. Equally important is the role of oxygen vacancies in phenomena such as fatigue and degradation in electroceramics, including ferroelectrics and high-*k* dielectrics[5].

Complementing the research in solid-state ionics, in the past three years there has been a rapidly growing appreciation of the role of oxygen-vacancy dynamics in the physics of transition-metal oxides[6], including magnetic, electronic, orbital and transport properties. A number of recent studies exemplify the role of surface electrochemistry on metal–insulator transitions in the $LaAlO_3$–$SrTiO_3$ system[7,8] and ferroelectric phase stability in perovskites[6,9,10]. Recent studies illustrating that vacancies can be mobile in the bulk at room temperature, severely affecting materials behaviour, underscore their importance in multiple other processes[11,12]. Overall, the role of vacancies in the physics and applications of oxide materials is comparable to the role of electrons and holes in classical semiconductor systems.

As with carrier concentrations across semiconductor interfaces, vacancy distributions can be non-uniform, with examples ranging from micrometre-scale gradients in solid-oxide fuel cells to nanometre-scale segregation of vacancies at interfaces and in the vicinity of defects. The capability to quantify vacancy distributions on the unit-cell level could help realize the full potential of oxide materials and devices and elucidate the physical phenomena at oxide surfaces and interfaces. Whereas the atomic and electronic structure of materials has become readily accessible through aberration-corrected scanning transmission electron microscopy[13] (STEM) and mapping of order-parameter fields such as polarization[14–18] and octahedral tilts[14,15,19] has recently become feasible, direct imaging and quantification of oxygen vacancies has remained a challenge. Although some reports of local vacancy concentration measurements through matching observed intensities to high-resolution transmission electron microscopy simulations at a grain boundary[20] and tracking electron energy-loss spectroscopy (EELS) fine structure in reduced $SrTiO_3$ (ref. 21) have been published, neither of these approaches proved to be sufficiently general to develop into a quantitative tool.

Here, we report quantitative mapping of local oxygen concentrations in ionic oxides and visualization of the oxygen vacancy distributions on the unit-cell level in the vicinity of interfaces based on direct mapping of vacancy-induced lattice expansion. The veracity of this approach is supported by density functional theory (DFT) calculations. In combination with chemically specific spectroscopic information, the present study opens a pathway for addressing the interplay between local ionic and physical phenomena and elucidating contributions of defects to the properties of oxygen transport.

[1]Materials Science and Technology Division, Oak Ridge National Laboratory, Oak Ridge, Tennessee 37831, USA, [2]Division of Electron Microscopic Research, Korea Basic Science Institute, Daejeon 305-333, South Korea, [3]Department of Physics and Astronomy, Vanderbilt University, Nashville, Tennessee 37235, USA, [4]Center for Nanophase Materials Sciences, Oak Ridge National Laboratory, Oak Ridge, Tennessee 37831, USA, [5]Spallation Neutron Source, Neutron Science Division, Oak Ridge National Laboratory, Oak Ridge, Tennessee 37831, USA, [6]Department of Electrical Engineering and Computer Science, Vanderbilt University, Nashville, Tennessee 37235, USA. *e-mail: albinab@ornl.gov.

© 2012 Macmillan Publishers Limited. All rights reserved.

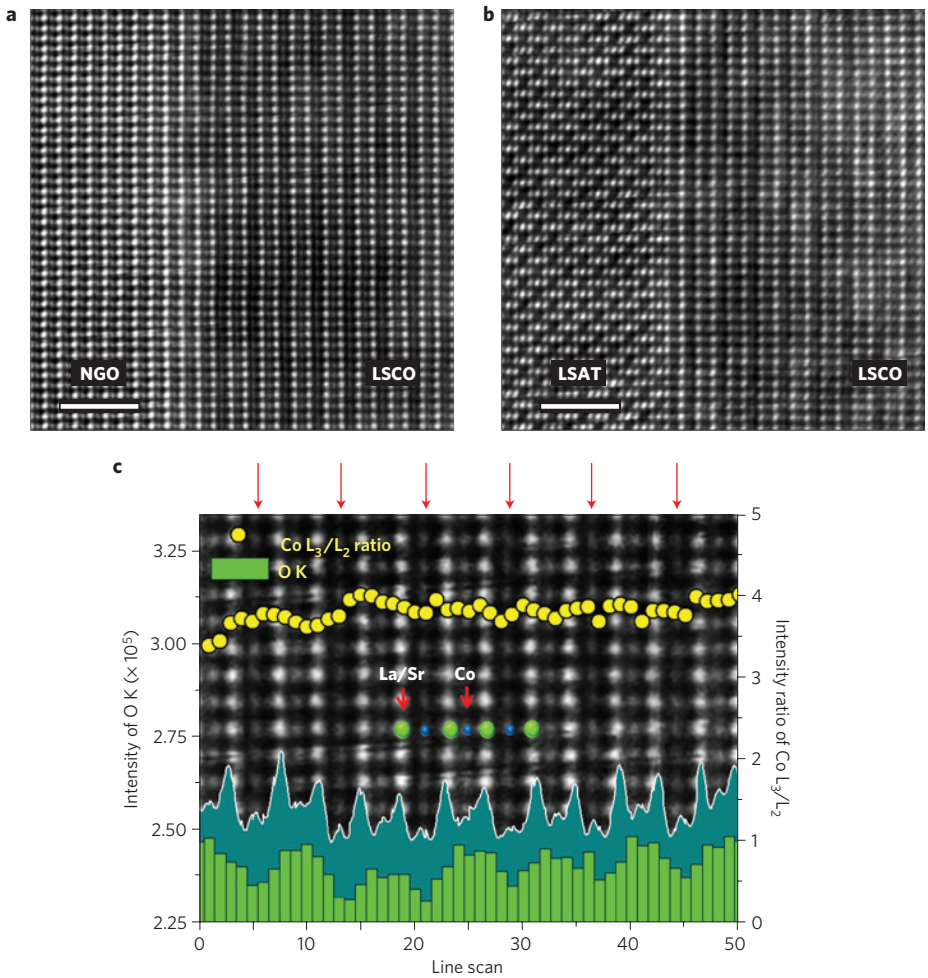

Figure 1 | Thin-film structures and the STEM–EELS analysis. a,**b**, ADF images of $[110]_c$-oriented LSCO thin films grown on different substrates, NGO (**a**) and LSAT (**b**). **c**, A representative STEM–EELS result for a bulk region of the LSCO film grown on NGO substrate. The alternating dark contrast (marked as red arrows) in every other Co–O plane results from the structural relaxation due to oxygen vacancy ordering in the planes (green bar graph shows O K edge intensity oscillation); an intensity modulation can also be seen in the overlaid line trace of the ADF signal (teal graph). The Co L_3/L_2 ratio (yellow circles) does not show significant modulations. Scale bars, 2 nm.

As a model system, we have chosen the $(La_{0.5}Sr_{0.5})CoO_{3-\delta}$ (LSCO) thin films grown on two different substrates: $NdGaO_3$ (NGO) and $(LaAlO_3)_{0.3}(Sr_2AlTaO_6)_{0.7}$ (LSAT). This system offers an advantage of well-understood structural defect chemistry[22,23], known electrochemical activity[24–26] and known relationship between electronic and ionic properties[27]. The vacancies in this material order in the brownmillerite structure, a process associated with strong relaxation of atomic positions giving rise to well-explored contrast in STEM (refs 28–31). The vacancy-ordered phases seem to behave similarly to ferroelastic materials, forming ordered domains with dissimilar orientations separated by twin and antiphase boundaries[31]. The NGO and LSAT substrates have almost identical lattice parameters, but strongly dissimilar octahedral tilt patterns[32,33] (tilted $a^-a^-c^+$ for NGO (ref. 34) and untilted $a^0a^0a^0$ for LSAT).

The typical thin-film structures for the two LSCO films along the $[110]_c$ (subscript c denotes pseudo-cubic) orientation are shown in annular dark-field (ADF) images (Fig. 1a,b). In this imaging mode, the atomic column intensity is approximately proportional to Z^2, where Z is the atomic number, whereby the bright columns are the cations and the lightest atomic columns containing oxygen contribute negligibly to the image intensity[35]. The LSCO thin films exhibit characteristic unit-cell doubling due to the ordering of oxygen vacancies in alternate (001) planes that cause displacements of cation columns[31]. In ADF STEM images, the oxygen-deficient planes are dimmer when compared with the stoichiometric planes, so the overall contrast seems modulated (Fig. 1a,b and Supplementary Fig. S1). This behaviour is common to other oxygen-vacancy-ordered materials including cobaltites, ferrites, manganites and even cuprates[28,31,36–38]. However, the observation of modulated contrast does not provide quantitative information on the oxygen content within individual layers, that is, quantitative values of $x1$ and $x2$ in the layer sequence $(La_{0.5}Sr_{0.5}O)$–CoO_{x1}–$(La_{0.5}Sr_{0.5}O)$ – CoO_{x2}. Here, we explore the approach for determining absolute stoichiometry $x1, x2$ based on EELS and direct measurements of the lattice parameter, extrapolating the concept of chemical expansivity[39–41] from the macroscopic to the unit-cell level.

Figure 1c illustrates EELS data from a bulk region of a LSCO/NGO film with vacancy ordering. The O K edge intensity recorded simultaneously with the ADF signal was reduced in the non-stoichiometric layers concurrently with the ADF contrast (see the green column graph). The integrated intensity of the O K EELS edge between the stoichiometric and oxygen-depleted layers differs by $3.9 \pm 0.7\%$. This, however, cannot be directly translated into local stoichiometry; for example, EELS intensity (proportional to the fraction of forward-scattered electrons) will increase as the ADF intensity (electrons scattered to high angles) decreases, thus

© 2012 Macmillan Publishers Limited. All rights reserved.

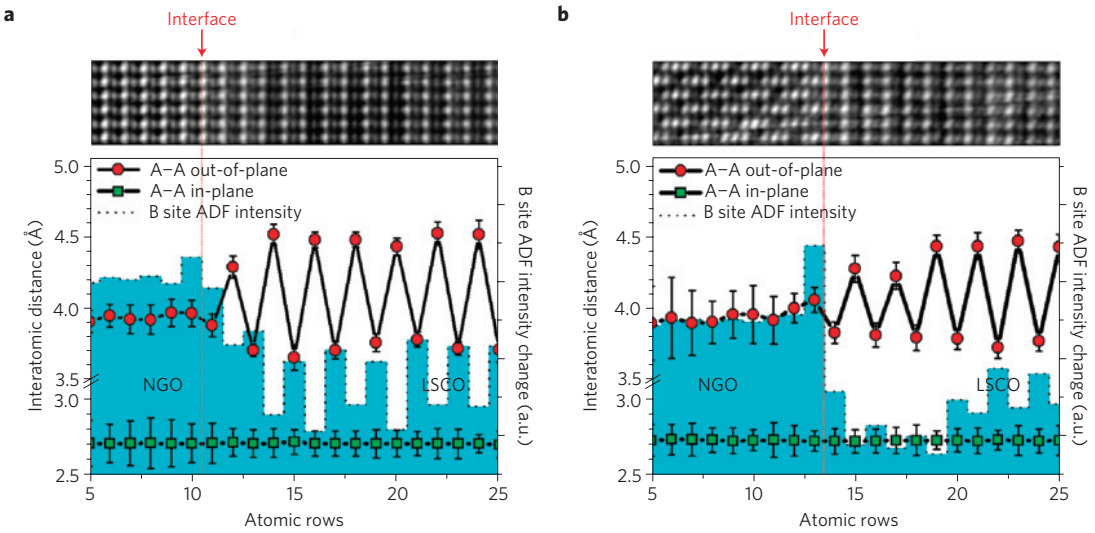

Figure 2 | Lattice spacing mapping from ADF STEM images. a,b, Top-most images on both sides are portions of ADF STEM images of LSCO on NGO (**a**) and LSCO on LSAT (**b**) taken in the pseudo-cubic [110] zone axis orientation. The graphs at the bottom of each image show atomic spacings along the out-of-plane (solid circles) and in-plane (solid squares) directions, averaged over vertical atomic rows of the images. The error bars show the standard deviation with respect to averaging for each (vertical) atomic layer in the image. The position of the interface can be tracked by the B-site cation ADF intensities across the interface (cyan bar graphs). Before quantification, STEM images were de-noised using Wiener filtering (HREM-Filters software package, HREM Research).

artificially boosting the signal for darker layers and reducing the observable difference. Other factors such as nonlinear thickness dependence and complex delocalization behaviour further hinder direct interpretation of the EELS edge intensities[42].

Another approach to evaluate local composition is based on the EEL fine structure of transition-metal L edges. Figure 1c shows the intensity ratio of the L_3 to L_2 peaks of the Co $L_{2,3}$ edge across the ordered layers for the region away from the interface of the LSCO/NGO sample; the results are shown as yellow circles (the same behaviour was observed in a region away from the interface of the LSCO/LSAT film; see Supplementary Fig. S2). For the measured $L_{2,3}$ ratio, the valence state of Co can be estimated to be +2.5 (see Supplementary Fig. S3 for calibration data). It is almost uniform through the bulk of the film and does not change between stoichiometric and non-stoichiometric layers. According to previous reports, this behaviour is attributable to the metal-like electronic structure and strong delocalization of electrons in the film[28]. Therefore, for this material, local variations in oxygen content cannot be inferred from Co L_3/L_2 ratios[38].

We note that in oxides there is a strong link between vacancy concentration and molar volume of a compound, generally referred to as chemical expansivity[39–41]. Here, we demonstrate how this concept can be used to extract the local oxygen vacancy concentration. To this end, we first carried out unit-cell-by-unit-cell lattice spacing mapping in the out-of-plane (c axis) direction using aberration-corrected ADF STEM images for both LSCO films (Fig. 2a,b). This approach allows measurement of the cation atomic positions within a selected range of unit cells in the ADF image with picometre precision. The top-most images on both sides in Fig. 2 represent ADF STEM images taken at the $[110]_c$ direction of the two LSCO films on NGO and LSAT, respectively. Averaged profiles for the out-of-plane (solid circle) and the in-plane (solid square) lattice spacings are shown as well. LSCO/substrate interfaces in the two LSCO samples were well defined as highlighted by the ADF intensity of the B-site cations, which is shown as a column-type graph in Fig. 2. Note that oxygen vacancy ordering is clearly manifested in the modulations of the out-of-plane lattice spacings in the two LSCO films, whereas no change is observed along the in-plane direction as expected owing to epitaxial constraints.

The representative behaviour of the c-axis lattice spacings for the two LSCO samples averaged over 10 images each (taken in different areas of the sample) is shown in Fig. 3a. Whereas the stoichiometric layers have almost identical spacing, the oxygen-depleted layers in LSCO on NGO are ~7% longer than in LSCO on LSAT. The lattice spacing depends weakly on the separation from the interface, with the bulk structure of the film being established in just a few layers. We note that the dispersion of lattice spacings (marked as error bars) for oxygen-depleted layers on NGO and LSAT are significantly different, suggesting true inhomogeneity rather than measurement error for the film on LSAT. The film on NGO, conversely, seems to have a homogeneous composition and thus possibly a stable structure, which our measurements suggest is brownmillerite $La_{0.5}Sr_{0.5}CoO_{2.5}$.

A perovskite oxide can transform into a brownmillerite structure with decreasing oxygen partial pressure; this process can occur reversibly even at low temperature[36,37,43]. The brownmillerite structure exhibits oxygen vacancy ordering along the [100] pseudo-cubic direction, where every other CoO_2 plane becomes oxygen-depleted CoO_{2-x}, whereas the other half of the planes stays stoichiometric. For $x = 1$, all Co cations in the oxygen-depleted planes are tetrahedrally coordinated, whereas Co cations in the stoichiometric planes are octahedrally coordinated (Fig. 3b,c). A characteristic feature of the fully tetrahedral depleted layer is the Co ion shift by $[a \pm 1/16, b \pm 1/16, 0]$, resulting in the pairing of Co in the structure[44] (Supplementary Fig. S4). The projected value of the Co ion shift viewed along the [100] direction of brownmillerite is ~0.3 Å (Fig. 3b)[45]. Indeed, using aberration-corrected STEM, we imaged this structural feature in the LSCO film on NGO, and the mean spacing of the Co ion pair was measured to be 0.30 ± 0.07 Å. (see Fig. 3d). Therefore, in the LSCO film grown on NGO, oxygen-depleted layers are fully tetrahedral, corresponding to a composition of $La_{0.5}Sr_{0.5}CoO_{2.5}$. At the same time, for the LSCO film on LSAT no evidence for Co ion pairing was observed. Therefore, the oxygen-depleted layers in this film are not fully tetrahedral, and the oxygen content of the film is higher. Indeed, for LSCO/NGO, the measured lattice spacings of stoichiometric (3.73 ± 0.04 Å) and oxygen-depleted layers (4.53 ± 0.04 Å) were remarkably close to the structural parameters

© 2012 Macmillan Publishers Limited. All rights reserved.

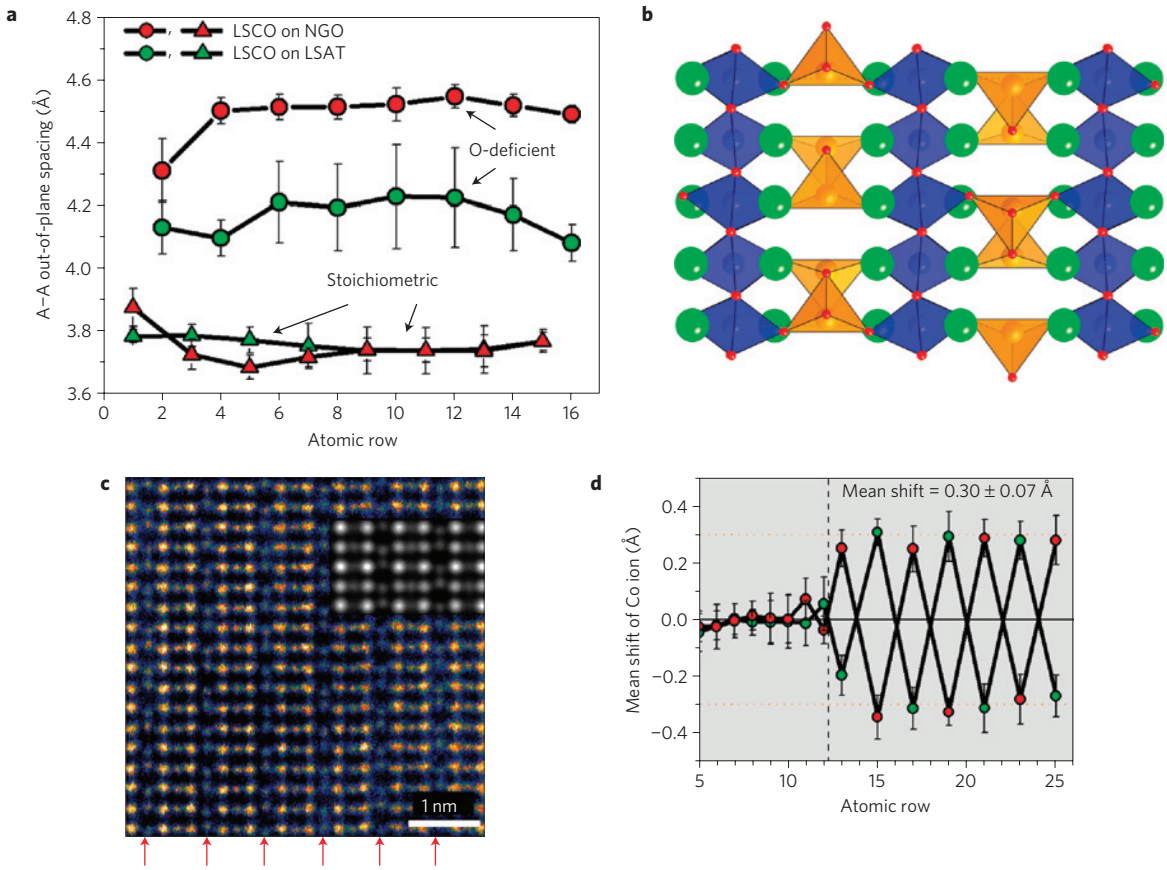

Figure 3 | Representative lattice spacing change and identified brownmillerite LSCO on NGO. a, Interatomic spacing changes of A-site cations in the two respective systems, LSCO on NGO (red) and LSCO on LSAT (green), along the *c* axis. The spacing changes for oxygen-deficient layers and stoichiometric layers in the structures are represented by solid circles and triangles, respectively. The error bars show the standard deviation with respect to averaging along the interface in multiple images (∼10 for each data set). **b**, Schematic of a brownmillerite structure $La_{0.5}Sr_{0.5}CoO_{2.5}$, where green spheres represent La/Sr atoms, blue spheres represent octahedral Co sites, orange spheres represent tetrahedral Co sites and small red spheres represent O atoms. Note the vertical shifts of Co in the tetrahedral layers. **c**, ADF STEM image of the $[100]_b$ (subscript b denotes brownmillerite)-oriented LSCO grown on NGO substrate showing the characteristic in-plane (vertical in the figure coordinates) pairwise shift of Co ions in the oxygen-depleted planes (solid arrows). The corresponding simulated image for the chemical composition of $La_{0.5}Sr_{0.5}CoO_{2.5}$ is given in the inset. **d**, Plot of the Co pairwise shift averaged over atomic rows of the LSCO film on NGO. The error bars show the standard deviation with respect to averaging for each (vertical) atomic layer in the image.

(3.783 and 4.527 Å, respectively) of the published brownmillerite structure for $La_{0.6}Sr_{0.4}MnO_{2.5}$ (orthorhombic, S.G.# 57)[46].

We therefore argue that the difference in lattice spacing can be interpreted as different populations of oxygen vacancies in the non-stoichiometric layer, that is, different **x** in AO–CoO_2–AO–CoO_x layer sequence along the *c* axis (axis of anisotropy). Oxygen-vacancy-induced chemical expansivity (β_c) at constant temperature (T) and partial pressure of oxygen (p_{O2}) can be expressed as a function of the mole fraction of oxygen vacancy (x), assumed to be macroscopically isotropic for a polycrystalline structure[39,43,47]. In the single-crystalline film with anisotropic vacancy ordering, β_c can be simplified as

$$\beta_c = \left(\frac{\partial \ln L_c}{\partial x}\right)_{T,p_{O2}}$$

where L_c is the lattice spacing along the axis of anisotropy. Using this definition, the total derivative of the anisotropic strain (ε_c) can be derived for a one-dimensional linear problem as

$$d\varepsilon_c(x)_{T,p_{O2}} = \beta_c \, dx$$

Thus, by measuring the anisotropic strain ($\Delta L_c/L_c$) as a function of the oxygen stoichiometry (x) on the atomic scale, we are able to determine β_c with high accuracy.

To verify this linear relationship at the subunit-cell level of a single layer, first-principles calculations based on DFT were performed using the Vienna *ab initio* Simulation Package code[48,49]. Five different compositions of the depleted layer were used, ranging from $x = 2$ (stoichiometric $La_{0.5}Sr_{0.5}CoO_3$) to $x = 1$ ($La_{0.5}Sr_{0.5}CoO_{2.5}$ brownmillerite), with intermediate points for $x = 1.75$, 1.50 and 1.25 (LSCO pseudo-cubic with oxygen vacancies distributed in the CoO_x layer). The results, along with a linear fit, are shown in Fig. 4a (marked as solid circles and a blue line). The lattice parameter expansion is obtained after the structures are fully relaxed along the *c* axis. The DFT modelling clearly demonstrates that the chemical expansivity can be scaled to the atomic level. Furthermore, chemical expansion is controlled by oxygen vacancy concentration regardless of whether the structure is a pseudo-cubic perovskite or brownmillerite (see the data at $x = 1.00$ in Fig. 4a). This result implies that interplanar spacing is directly related to oxygen content; that is, a simple measurement of the chemical expansion can be universally applied to determine the oxygen stoichiometry in both ordered and disordered oxygen-deficient materials (although oxygen vacancy ordering transitions change the symmetry of a material, they have a very small effect on the molar volume). This approach can also work for other situations where a set of structural models can be generated and theoretically examined, for example, for quantification of vacancy accumulation around a defect.

© 2012 Macmillan Publishers Limited. All rights reserved.

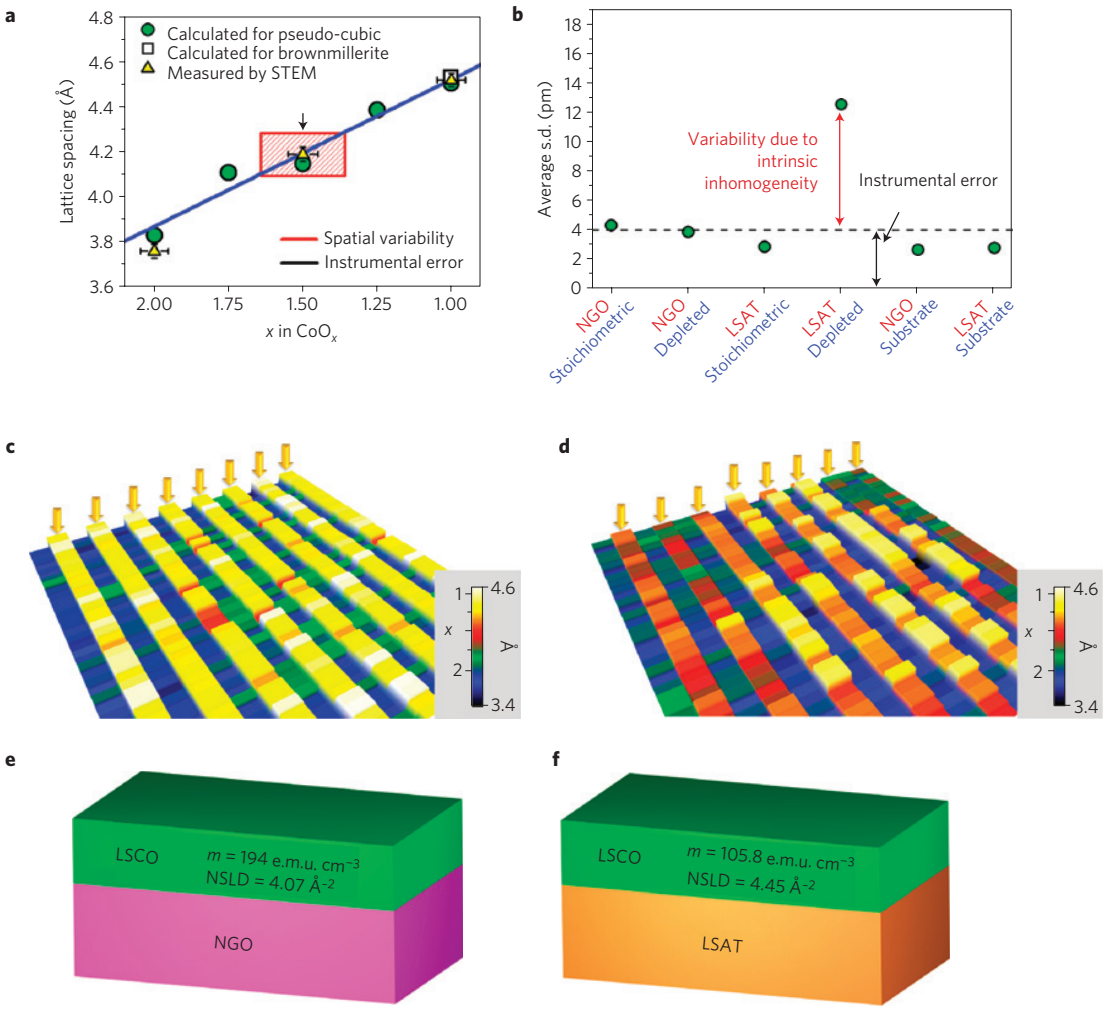

Figure 4 | Determination of oxygen content in LSCO. a, Lattice expansivity as a function of oxygen deficiency (x in CoO_x). A linear fit (solid blue line) was obtained from DFT calculations (marked as solid green circles) for five models with different oxygen contents from $x = 2$ (a stoichiometric Co–O layer in cubic perovskite) to $x = 1$ (for an oxygen-deficient layer in brownmillerite); variability for LSCO/LSAT layer spacing is due to both instrumental error (black error bars) and intrinsic inhomogeneity (red cross-hatched box). **b**, Average standard deviations of different lattice spacing measurements can be used to estimate the measurement error (see text) and separate the contribution due to inhomogeneity for LSCO/LSAT. **c**,**d**, Bird's eye views of out-of-plane lattice spacing mapping results for the respective LSCO/NGO and LSCO/LSAT systems. The local oxygen content for each system is directly visualized over the whole region imaged by STEM; note the higher inhomogeneity of the oxygen-deficient layer composition for LSCO/LSAT (Fig. 4d). The oxygen-deficient layers in both LSCO structures are marked as solid arrows. **e**,**f**, Results of the PNR data showing the reduction in the NSLD for the films on NGO, indicating an agreement with STEM observations. The PNR also shows the impact of the observed effects on magnetism, which is approximately twice as large for the films on NGO.

The experimental c-axis lattice spacings of the oxygen-depleted layer in the LSCO on NGO (4.53 ± 0.04 Å) and the stoichiometric layer (3.73 ± 0.04 Å) are shown in Fig. 4a as solid yellow triangles. These values show remarkable agreement with theoretical findings. We can therefore use the linear fit of the theoretical data as a calibration curve to determine the local oxygen content in the depleted LSCO layer on LSAT (spacing of 4.19 ± 0.13 Å; indicated in the Fig. 4a). The average oxygen stoichiometry of the LSCO on LSAT is thus projected to be $x = 1.5$ in CoO_x layer, corresponding to an overall $La_{0.5}Sr_{0.5}CoO_{2.75}$ composition. However, as was mentioned before, the increased scatter of the measured values for the CoO_x layers in LSCO on LSAT probably reflects not only measurement error, but also intrinsic inhomogeneity in oxygen distribution. Indeed, if we plot the average standard deviations (s.d.) of the different LSCO lattice spacings measured in this series of experiments, along with those for the substrate lattice spacings (Fig. 4b), the LSCO/LSAT depleted-layer measurement stands out with a s.d. more than triple the nearest value, whereas the rest of the measurements seem consistent. It is therefore reasonable to assume that the error in the determination of the mean composition for LSCO/LSAT is of the order of the measurement error of ± 4 pm on the basis of the data in Fig. 4b (Fig. 4a, black error bars). We can further use this data to estimate the range of local oxygen concentrations in this layer. For the measurement error of ± 4 pm, the spacing variability due to intrinsic inhomogeneity in the CoO_x layers in LSCO/LSAT is 4.19 ± 0.09 Å, translating into local depleted-layer compositions of $CoO_{1.36}$ to $CoO_{1.66}$.This range is shown in Fig. 4a as a red cross-hatched rectangle. Further statistical data are given in Supplementary Fig. S8.

In a similar way we can estimate overall sensitivity of our method to compositional variations. For the spacing measurement error of ± 4 pm, the error for the oxygen content in each layer is estimated to be $\pm \sim 4\%$. For the overall oxygen content (as per (La,Sr) $CoO_{3-\delta}$), if we assume, in agreement with published structural and theoretical data, that (La,Sr)O layers are fully oxygenated, the error is estimated to be $\pm \sim 3\%$. Given both the local and global sensitivity of our mea-

© 2012 Macmillan Publishers Limited. All rights reserved.

surement to the oxygen vacancy concentration, as shown in Fig. 4a, we can convert the lattice spacing maps into the oxygen vacancy distribution maps as shown in Fig. 4c,d. These bird's eye views of two regions of LSCO films grown on the respective NGO and LSAT substrates visually demonstrate the highly ordered and homogeneous distribution of oxygen vacancies in the brownmillerite LSCO (Fig. 4c), whereas the pseudo-cubic perovskite LSCO shows significant inhomogeneity, consistent with our reasoning above (Fig. 4d).

Remarkably, LSCO films grown on two different substrates with similar epitaxial strain exhibit different oxygen stoichiometry. Long-range chemical intermixing with the substrate is unlikely at a growth temperature of 650 °C considering that the substrates have melting points of 2,110 K for LSAT and 1,600 K for NGO, and no evidence of intermixing is seen in Fig. 2a,b. Furthermore, both NGO and LSAT are extremely poor oxygen conductors, rendering their oxygen supply kinetically inaccessible to the film during growth, ruling out any effect of substrate chemical potential. Hence, we conclude that it is the dissimilar octahedral tilt patterns (tilted $a^-a^-c^+$ for NGO and untilted $a^0a^0a^0$ for LSAT) that are the primary cause for this oxygen stoichiometry difference. Although these changes may be influenced by the fact that STEM studies are carried out in vacuum (from diffusion considerations[50], it is possible that the oxygen stoichiometry can reach its equilibrium value within the timescale of the experiment), the observed difference in oxygen chemical potential should also have implications at ambient pressure.

To explore the impact of the different substrates on the macroscopic film properties, in particular magnetism, we used polarized neutron reflectometry (PNR), which allows simultaneous measurement of magnetization and structural scattering density with the depth resolution of 0.5 nm (ref. 51). Low-temperature PNR measurements were carried out on the MAGICS Reflectometer at the Spallation Neutron Source at Oak Ridge National Laboratory. From the quantitative analysis with the simultaneous fit to the experimental reflectivities measured for the two neutron polarizations, the depth profiles of the nuclear and magnetic scattering length densities of the films were obtained. The measurements indicate that the nuclear scattering length density (NSLD) inside the LSCO film for the LSCO/NGO sample (4.07 A^{-2}) is lower than that for the LSCO/LSAT sample (4.45 A^{-2}; see schematics in Fig. 4e,f), even though macroscopic X-ray measurements did not detect significant enhancement of the c-axis lattice parameter in these films. Given that the NSLD is determined by the number of atoms with a different scattering length per unit volume, a deficiency of oxygen as determined by the microscopy data agrees with the reduction of the NSLD of the LSCO/NGO sample. Another result from the PNR data is that the magnetization inside the LSCO film for the LSCO/NGO sample (194 e.m.u. cm^{-3}) is significantly higher than that for the LSCO/LSAT sample (105.8 e.m.u. cm^{-3}; Fig. 4e,f), demonstrating that the different structure of these samples affects the macroscopic material properties.

We demonstrate a new paradigm for mapping oxygen vacancy concentrations in ordered and disordered perovskites with high accuracy and efficiency, expanding the concept of chemical expansivity to the subunit-cell level. Furthermore, we demonstrate that the tilt effect imposed by substrate symmetry can influence the overall oxygen stoichiometry in the film. These studies will be of direct interest for the exploration of solid-oxide fuel-cell materials and devices, as well as for understanding the general physics of oxide materials and interfaces.

Method

Thin-film synthesis and STEM sample preparations. The LSCO thin films were grown on different substrates, NGO and LSAT, by pulsed laser deposition under identical processing conditions with 200 mtorr O_2 at 650 °C and remained in oxidation ambience with 200 torr O_2 gas down to room temperature. The NGO substrate has an orthorhombic structure with tilted BO_6 octahedra ($a^-a^-c^+$ in Glazer's notation[32]), whereas the LSAT substrate has a cubic structure with an untilted $a^0a^0a^0$ structure. These substrates have nearly identical lattice parameters of $a = 3.861$ (average, 3.864 average in-plane) for NGO and 3.868 Å for LSAT, less than 0.2% difference. From the X-ray diffraction measurements, the LSCO films on the two substrates showed different symmetries, which resulted from the substrate-imposed octahedral tilts, giving tetragonal and orthorhombic structures when grown epitaxially on LSAT and NGO, respectively. Samples for STEM analysis were prepared in cross-sections oriented along the ⟨100⟩ and ⟨110⟩ pseudo-cubic directions using precision polishing followed by Ar ion milling.

STEM imaging and analysis. ADF STEM images for samples were recorded using aberration-corrected scanning transmission electron microscopes (VG Microscopes HB603U operating at 300 kV and Nion UltraSTEM operating at 100 kV). EELS experiments were performed with a Gatan Enfina electron energy loss spectrometer attached to the VG Microscopes HB603U. The thicknesses of the observed regions were estimated to be about 50 nm or less by measuring the intensity ratio between the plasmon loss and the zero-loss peaks in EELS. Noise in the obtained STEM images was reduced by using Wiener filtering (HREM-Filters software package by HREM Research). Atom coordinates were determined using a centre-of-mass refinement method. The lattice spacing measurements are reproducible and robust in the experimental conditions used for the study (Supplementary Figs S5 and S6). Observations of films in the $[100]_c$ orientation (see Supplementary Fig. S7) show that vacancy ordering in these systems occurs only in the $[001]_c$ direction, unlike the case of ref. 28, where ordering in both the $[001]_c$ and $[010]_c$ directions was detected.

DFT calculations. For the structural relaxation calculations, we have used a first-principles plane-wave density-functional method and a projector augmented-wave potential implemented in the Vienna *ab initio* Simulation Package. The spin-polarized generalized-gradient approximation is applied to the ground-state structures of $La_{0.5}Sr_{0.5}CoO_3$ (cubic, space group $Pm\bar{3}m$), $La_{0.5}Sr_{0.5}CoO_{2.5}$ (brownmillerite, space group Pcmb) and LSCO (pseudo-cubic, space group $P4/mmm$). The Sr doping is considered by the substitution of Sr at La sites with a ratio of 1:1 in a rocksalt configuration. The magnetic states are relaxed in collinear configurations.

PNR. PNR experiments were conducted at the SNS at Oak Ridge National Laboratory, using the Magnetism Reflectometer MAGICS. This is a time-of-flight instrument with a wavelength band in the 0.2–0.5 nm range, and a polarization efficiency of 98%. The experiments were conducted at a temperature of 6 K. PNR is a non-destructive method to determine scattering length density profiles. Neutrons interact with both nuclei and the atomic magnetic moment. Neutrons with the opposite spin projections on the direction of the magnetic moment interact with the same nuclear scattering potential, whereas the magnetic scattering potential enters with the opposite sign. Subsequent measurement with a neutron beam polarized along and opposite to the external field allowed for an independent determination of the reflectivities $R+$ and $R-$ so that the two contributions could be separated to reconstruct the depth profiles of the chemical structure and the magnetization vector.

Received 8 February 2012; accepted 4 July 2012; published online 19 August 2012

References

1. Adler, S. B. Factors governing oxygen reduction in solid oxide fuel cell cathodes. *Chem. Rev.* **104,** 4791–4843 (2004).
2. Minh, N. Q. Ceramic fuel-cells. *J. Am. Ceram. Soc.* **76,** 563–588 (1993).

© 2012 Macmillan Publishers Limited. All rights reserved.

3. Sawa, A. Resistive switching in transition metal oxides. *Mater. Today* **11,** 28–36 (June 2008).
4. Waser, R., Dittmann, R., Staikov, G. & Szot, K. Redox-based resistive switching memories—nanoionic mechanisms, prospects, and challenges. *Adv. Mater.* **21,** 2632–2663 (2009).
5. Tagantsev, A. K., Stolichnov, I., Colla, E. L. & Setter, N. Polarization fatigue in ferroelectric films: Basic experimental findings, phenomenological scenarios, and microscopic features. *J. Appl. Phys.* **90,** 1387–1402 (2001).
6. Wang, R. V. *et al.* Reversible chemical switching of a ferroelectric film. *Phys. Rev. Lett.* **102,** 047601 (2009).
7. Bi, F. *et al.* Water-cycle mechanism for writing and erasing nanostructures at the $LaAlO_3/SrTiO_3$ interface. *Appl. Phys. Lett.* **97,** 173110 (2010).
8. Bristowe, N. C., Littlewood, P. B. & Artacho, E. Surface defects and conduction in polar oxide heterostructures. *Phys. Rev. B* **83,** 205405 (2011).
9. Kalinin, S. V., Johnson, C. Y. & Bonnell, D. A. Domain polarity and temperature induced potential inversion on the $BaTiO_3$(100) surface. *J. Appl. Phys.* **91,** 3816–3823 (2002).
10. Stephenson, G. B. & Highland, M. J. Equilibrium and stability of polarization in ultrathin ferroelectric films with ionic surface compensation. *Phys. Rev. B* **84,** 064107 (2011).
11. Jiang, W. *et al.* Mobility of oxygen vacancy in $SrTiO_3$ and its implications for oxygen-migration-based resistance switching. *J. Appl. Phys.* **110,** 034509 (2011).
12. Yi, H. T., Choi, T., Choi, S. G., Oh, Y. S. & Cheong, S. W. Mechanism of the switchable photovoltaic effect in ferroelectric $BiFeO_3$. *Adv. Mater.* **23,** 3403–3407 (2011).
13. Pennycook, S. J., Varela, M., Lupini, A. R., Oxley, M. P. & Chisholm, M. F. Atomic-resolution spectroscopic imaging: Past, present and future. *J. Electron Microsc.* **58,** 87–97 (2009).
14. Borisevich, A. *et al.* Mapping octahedral tilts and polarization across a domain wall in $BiFeO_3$ from Z-contrast scanning transmission electron microscopy image atomic column shape analysis. *ACS Nano* **4,** 6071–6079 (2010).
15. Borisevich, A. Y. *et al.* Suppression of octahedral tilts and associated changes in electronic properties at epitaxial oxide heterostructure interfaces. *Phys. Rev. Lett.* **105,** 087204 (2010).
16. Chang, H. J. *et al.* Atomically resolved mapping of polarization and electric fields across ferroelectric/oxide interfaces by Z-contrast imaging. *Adv. Mater.* **23,** 2474–2479 (2011).
17. Jia, C. L. *et al.* Atomic-scale study of electric dipoles near charged and uncharged domain walls in ferroelectric films. *Nature Mater.* **7,** 57–61 (2008).
18. Jia, C. L. *et al.* Unit-cell scale mapping of ferroelectricity and tetragonality in epitaxial ultrathin ferroelectric films. *Nature Mater.* **6,** 64–69 (2007).
19. Jia, C. L. *et al.* Oxygen octahedron reconstruction in the $SrTiO_3/LaAlO_3$ heterointerfaces investigated using aberration-corrected ultrahigh-resolution transmission electron microscopy. *Phys. Rev. B* **79,** 081405 (2009).
20. Jia, C. L., Lentzen, M. & Urban, K. Atomic-resolution imaging of oxygen in perovskite ceramics. *Science* **299,** 870–873 (2003).
21. Muller, D. A., Nakagawa, N., Ohtomo, A., Grazul, J. L. & Hwang, H. Y. Atomic-scale imaging of nanoengineered oxygen vacancy profiles in $SrTiO_3$. *Nature* **430,** 657–661 (2004).
22. Ivanova, N. B., Ovchinnikov, S. G., Korshunov, M. M., Eremin, I. M. & Kazak, N. V. Specific features of spin, charge, and orbital ordering in cobaltites. *Phys. Usp.* **52,** 789–810 (2009).
23. Petrov, A. N., Cherepanov, V. & Zuev, A. Y. Thermodynamics, defect structure, and charge transfer in doped lanthanum cobaltites: An overview. *J. Solid State Electrochem.* **10,** 517–537 (2006).
24. Crumlin, E. J. *et al.* Oxygen reduction kinetics enhancement on a heterostructured oxide surface for solid oxide fuel cells. *J. Phys. Chem. Lett.* **1,** 3149–3155 (2010).
25. La O, G. J. *et al.* Catalytic activity enhancement for oxygen reduction on epitaxial perovskite thin films for solid-oxide fuel cells. *Angew. Chem. Int. Ed.* **49,** 5344–5347 (2010).
26. Mutoro, E., Crumlin, E. J., Biegalski, M. D., Christen, H. M. & Shao-Horn, Y. Enhanced oxygen reduction activity on surface-decorated perovskite thin films for solid oxide fuel cells. *Energy Environ. Sci.* **4,** 3689–3696 (2011).
27. Lankhorst, M. H. R., Bouwmeester, H. J. M. & Verweij, H. Use of the rigid band formalism to interpret the relationship between O chemical potential and electron concentration in $La_{1-x}Sr_xCoO_{3-\delta}$. *Phys. Rev. Lett.* **77,** 2989–2992 (1996).
28. Gazquez, J. *et al.* Atomic-resolution imaging of spin-state superlattices in nanopockets within cobaltite thin films. *Nano Lett.* **11,** 973–976 (2011).
29. Gspan, C. *et al.* Crystal structure of $La_{(0.4)}Sr_{(0.6)}CoO_{(2.71)}$ investigated by TEM and XRD. *J. Solid State Chem.* **181,** 2976–2982 (2008).
30. Klenov, D. O., Donner, W., Foran, B. & Stemmer, S. Impact of stress on oxygen vacancy ordering in epitaxial $(La_{0.5}Sr_{0.5})CoO_{3-\delta}$ thin films. *Appl. Phys. Lett.* **82,** 3427–3429 (2003).
31. Klie, R. F., Ito, Y., Stemmer, S. & Browning, N. S. Observation of oxygen vacancy ordering and segregation in perovskite oxides. *Ultramicroscopy* **86,** 289–302 (2001).
32. Glazer, A. M. Classification of tilted octahedra in perovskites. *Acta Crystallogr. B* **28,** 3384–3392 (1972).
33. Rondinelli, J. M. & Spaldin, N. A. Structure and properties of functional oxide thin films: Insights from electronic-structure calculations. *Adv. Mater.* **23,** 3363–3381 (2011).
34. Vasylechko, L. *et al.* The crystal structure of $NdGaO_3$ at 100 K and 293 K based on synchrotron data. *J. Alloys Compounds* **297,** 46–52 (2000).
35. Pennycook, S. J. & Nellist, P. D. (eds) *Scanning Transmission Electron Microscopy* (Springer, 2011).
36. Ferguson, J. D. *et al.* Epitaxial oxygen getter for a brownmillerite phase transformation in manganite films. *Adv. Mater.* **23,** 1226–1230 (2011).
37. Inoue, S. *et al.* Anisotropic oxygen diffusion at low temperature in perovskite-structure iron oxides. *Nature Chem.* **2,** 213–217 (2010).
38. Tao, J. *et al.* Direct imaging of nanoscale phase separation in $La_{0.55}Ca_{0.45}MnO_3$: Relationship to colossal magnetoresistance. *Phys. Rev. Lett.* **103,** 097202 (2009).
39. Adler, S. B. Chemical expansivity of electrochemical ceramics. *J. Am. Ceram. Soc.* **84,** 2117–2119 (2001).
40. Kharton, V. V., Marques, F. M. B. & Atkinson, A. Transport properties of solid oxide electrolyte ceramics: A brief review. *Solid State Ion.* **174,** 135–149 (2004).
41. Morozovska, A. N. *et al.* Thermodynamics of electromechanically coupled mixed ionic-electronic conductors: Deformation potential, Vegard strains, and flexoelectric effect. *Phys. Rev. B* **83,** 195313 (2011).
42. Oxley, M. P. & Pennycook, S. J. Image simulation for electron energy loss spectroscopy. *Micron* **39,** 676–684 (2008).
43. Chen, X. Y., Yu, J. S. & Adler, S. B. Thermal and chemical expansion of Sr-doped lanthanum cobalt oxide $(La_{1-x}Sr_xCoO_{3-\delta})$. *Chem. Mater.* **17,** 4537–4546 (2005).
44. Stemmer, S., Jacobson, A. J., Chen, X. & Ignatiev, A. Oxygen vacancy ordering in epitaxial $La_{0.5}Sr_{0.5}CoO_{3-\delta}$ thin films on (001) $LaAlO_3$. *J. Appl. Phys.* **90,** 3319–3324 (2001).
45. Ito, Y., Klie, R. F. & Browning, N. S. Atomic resolution analysis of the defect chemistry and microdomain structure of brownmillerite-type strontium cobaltite. *J. Am. Ceram. Soc.* **85,** 969–976 (2002).
46. Parsons, T. G., D'Hondt, H., Hadermann, J. & Hayward, M. A. Synthesis and structural characterization of $La_{1-x}A_xMnO_{2.5}$ (A = Ba, Sr, Ca) phases: Mapping the variants of the brownmillerite structure. *Chem. Mater.* **21,** 5527–5538 (2009).
47. Tsipis, E. V. *et al.* Oxygen deficiency, vacancy clustering and ionic transport in $(La,Sr)Co\ O_{3-\delta}$. *Solid State Ion.* **192,** 42–48 (2011).
48. Kohn, W. & Sham, L. J. Self-consistent equations including exchange and correlation effects. *Phys. Rev.* **140,** A1133–A1138 (1965).
49. Kresse, G. & Furthmüller, J. Efficient iterative schemes for *ab initio* total-energy calculations using a plane-wave basis set. *Phys. Rev. B* **54,** 11169–11186 (1996).
50. De Souza, R. A. & Kilner, J. A. Oxygen transport in $La_{(1-x)}Sr_{(x)}Mn_{(1-y)}Co_{(y)}O_{(3+/-\delta)}$ perovskites—part I. Oxygen tracer diffusion. *Solid State Ion.* **106,** 175–187 (1998).
51. Lauter, V., Ambaye, H., Goyette, R., Hal Lee, W-T. & Parizzi, A. Highlights from the magnetism reflectometer at the SNS. *Physica B* **404,** 2543–2546 (2009).

Acknowledgements

The work was supported by the Materials Science and Engineering Division of the US DOE. Portions of this research were conducted at the Center for Nanophase Materials Sciences and the Spallation Neutron Source, which are both sponsored at Oak Ridge National Laboratory by the Scientific User Facilities Division, Office of Basic Energy Sciences, US Department of Energy. The authors are grateful to D. Morgan (U. Wisc) for valuable advice.

Author contributions

Y-M.K. and A.Y.B. collected and analysed the STEM data, M.D.B. and H.M.C. grew the samples, H.A., V.L. and M.D.B. collected and analysed the PNR data, and J.H. and S.T.P. performed the DFT calculations. All authors contributed to writing the paper. A.Y.B. and S.V.K. conceived and coordinated the project.

Additional information

Supplementary information is available in the online version of the paper. Reprints and permissions information is available online at www.nature.com/reprints. Correspondence and requests for materials should be addressed to A.Y.B.

Competing financial interests

The authors declare no competing financial interests.

© 2012 Macmillan Publishers Limited. All rights reserved.